Astronomy & Astrophysics manuscript no. output
May 4, 2026

GA-NIFS: AGN activity in a Lyα emitter within a triple-AGN system anchored by a passive galaxy at $z = 3$

Michele Perna[1]⋆, Santiago Arribas[1], Mahmoud Hamed[1], Francesco D'Eugenio[2,3], Isabella Lamperti[4,5], Andrew J. Bunker[6], Stefano Carniani[7], Stéphane Charlot[8], Roberto Maiolino[2,3,9], Bruno Rodríguez Del Pino[1], Hannah Übler[10], Torsten Böker[11], Elena Bertola[5], Giovanni Cresci[5], Giacomo Venturi[7], Michele Ginolfi[4,5], Montserrat Villar Martín[1], and Sandra Zamora[7]

[1] Centro de Astrobiología (CAB), CSIC–INTA, Cra. de Ajalvir Km. 4, 28850 – Torrejón de Ardoz, Madrid, Spain
[2] Kavli Institute for Cosmology, University of Cambridge, Madingley Road, Cambridge, CB3 0HA, UK
[3] Cavendish Laboratory - Astrophysics Group, University of Cambridge, 19 JJ Thomson Avenue, Cambridge, CB3 0HE, UK
[4] Università di Firenze, Dipartimento di Fisica e Astronomia, via G. Sansone 1, 50019 Sesto F.no, Firenze, Italy
[5] INAF - Osservatorio Astrofisico di Arcetri, Largo E. Fermi 5, I-50125 Firenze, Italy
[6] Department of Physics, University of Oxford, Denys Wilkinson Building, Keble Road, Oxford OX1 3RH, UK
[7] Scuola Normale Superiore, Piazza dei Cavalieri 7, I-56126 Pisa, Italy
[8] Sorbonne Université, CNRS, UMR 7095, Institut d'Astrophysique de Paris, 98 bis bd Arago, 75014 Paris, France
[9] Department of Physics and Astronomy, University College London, Gower Street, London WC1E 6BT, UK
[10] Max-Planck-Institut für extraterrestrische Physik (MPE), Gießenbachstraße 1, 85748 Garching, Germany
[11] European Space Agency, c/o STScI, 3700 San Martin Drive, Baltimore, MD 21218, USA

Received September 15, 1996; accepted March 16, 1997

ABSTRACT

Context. Massive quenched galaxies at $z > 3$ challenge models of early galaxy evolution, as their rapid formation and abrupt quenching require efficient feedback, which is often linked to active galactic nuclei (AGNs). The quiescent galaxy GS10578 at $z = 3.064$ is a key example of this population. Previous JWST/NIRSpec integral field unit (IFU) observations revealed an AGN-driven outflow and uncovered a compact pair of AGNs separated by ~ 5 kpc. In addition, VLT/MUSE spectroscopy identified a third AGN candidate at a projected distance of ~ 30 kpc, associated with a luminous Lyα emitter (LAE2) characterised by high-ionisation UV lines, although rest-frame optical diagnostics were not previously available.
Aims. We aim to confirm the nature of LAE2 using rest-frame optical diagnostics enabled by new JWST observations, and to characterise the physical and ionisation properties of both LAE2 and a distinct nearby Lyα emitter (LAE1) that lacks any detectable continuum counterpart. Through this analysis, we investigated the interplay among low-mass satellites, black-hole growth, and the ionised environment of a quenched massive galaxy at high redshift.
Methods. We analysed new JWST/NIRSpec IFU observations targeting the optical nebular lines of LAE1 and LAE2, including Hβ, [O III], Hα, and [N II], complemented with VLT/MUSE IFU spectroscopy, as part of the GA-NIFS project. We extracted integrated and spatially resolved spectra, constructed emission-line maps, and used standard diagnostic diagrams to determine ionisation sources and kinematics.
Results. LAE2 exhibits rest-frame UV–optical-line ratios fully consistent with an embedded AGN. Its [O III] and Hα emission displays a clumpy morphology and irregular, non-rotating kinematics on sub-kiloparsec scales. Except for Lyα, LAE1 remains undetected in all nebular lines and in JWST imaging; its Lyα emission is broad ($\sigma \sim 200$ km s^{-1}) and asymmetric. The similarity of the LAE1 and LAE2 Lyα profiles in both velocity and flux suggests that LAE1 traces resonantly scattered emission powered by LAE2 rather than in situ star formation (although the latter cannot be completely ruled out).
Conclusions. Our analysis reveals that the environment of GS10578 contains both multi-black-hole activity and gas structures on tens-of-kiloparsec scales, offering new insights into how feedback, accretion, and satellite interactions influence the late evolutionary stages of quenched massive galaxies.

Key words. galaxies: high-redshift – galaxies: interactions – galaxies: ISM

1. Introduction

Rapid galaxy formation and subsequent cessation of star formation (quenching) in massive quiescent galaxies shortly after the Big Bang ($z \gtrsim 3$, 1–2 Gyr before cosmic noon) pose a major challenge to models of galaxy evolution (e.g. Glazebrook et al. 2017, 2024; Boylan-Kolchin 2023; Carnall et al. 2023; Valentino et al. 2023; Baker et al. 2025; de Graaff et al. 2025; McConachie et al. 2025; Weibel et al. 2025). Understanding the mechanism responsible for removing cool gas (i.e. the fuel for star formation) or preventing its supply is crucial. Current theory favours cumulative feedback from central supermassive black holes (SMBHs), which can act either through ejective mechanisms (removing gas via outflows; e.g. King & Pounds 2015; Xie et al. 2024) or preventative mechanisms (stopping fresh accretion; e.g. Croton et al. 2006; Zinger et al. 2020; Bluck et al. 2022).

The *James Webb* Space Telescope (JWST), particularly with the Near-InfraRed Spectrograph (NIRSpec) in its integral field

⋆ e-mail: mperna@cab.inta-csic.es

Article published by EDP Sciences, to be cited as https://doi.org/10.1051/0004-6361/202658847

spectroscopic (IFS) mode (Böker et al. 2022; Jakobsen et al. 2022), has begun to probe these monumental galaxies during this key evolutionary epoch (e.g. Pérez-González et al. 2025; Pascalau et al. 2026). The galaxy GS10578 at $z = 3.064$ is an excellent laboratory for studying quenching processes. It is a highly massive system ($M_\star \approx 10^{11}$ $M_\odot$) classified as a quiescent galaxy, with a current star formation rate (SFR) estimated to be ≤ 6 $M_\odot$ yr^{-1} (D'Eugenio et al. 2024; Scholtz et al. 2026). GS10578 hosts an active galactic nucleus (AGN), confirmed by its X-ray detection ($L_X = 6.4\times10^{44}$ erg s^{-1}) and extreme position on the Baldwin, Phillips & Terlevich (BPT; Baldwin et al. 1981) emission-line-ratio diagnostic diagram (Perna et al. 2025). It is classified as a radio-quiet AGN, with $q24 = 0.49 \pm 0.03$ (with $q24$ defined as an observed ratio of 24 μm to radio luminosity) detected both at 3 and 6 GHz (4×10^{40} and 1×10^{40} erg s^{-1}, respectively; Lyu et al. 2022).

Direct evidence of AGN feedback in GS10578 has been established, demonstrating powerful neutral-gas outflows traced by Na ID absorption, with mass outflow rates ($\approx$ 30 – 100 $M_\odot$ yr^{-1}) significantly exceeding the estimated SFR, strongly supporting the dominance of ejective feedback in quenching the galaxy (D'Eugenio et al. 2024; see also Venturi et al. 2025). Furthermore, GS10578 exhibits ordered stellar rotation, suggesting that quenching occurred without destroying the galaxy's disc structure (D'Eugenio et al. 2024). The non-detection of CO(3-2) in deep (seven-hour integration) Atacama Large Millimetre/sub-millimetre Array (ALMA) observations surprisingly reveals that the galaxy has a cold molecular gas mass of $M_{mol} < 10^{9.1}$ $M_\odot$; this represents one of the most stringent upper limits on the gas mass for a quiescent galaxy at high redshift (Scholtz et al. 2026).

Recent JWST/NIRSpec IFS and JWST/NIRCam imaging, together with archival optical observations with the IFS Multi Unit Spectroscopic Explorer (MUSE) at the Very Large Telescope (VLT), have revealed that GS10578 resides in a complex, dense environment, potentially harbouring a triple-AGN system (Perna et al. 2025). In addition to the primary AGN in GS10578 (AGN-A) and a close companion that also hosts an active nucleus (AGN-B; 4.7 kpc separation) on the basis of optical-line diagnostics, the system includes multiple gas-rich satellites detected in NIRCam medium-band filters covering the [O III] emission (D'Eugenio et al. 2024), and two Lyα Emitters (LAEs) detected in VLT/MUSE data (Perna et al. 2025; see also Fig. 1). These two sources are situated at a projected separation of $\approx$ 30 kpc from the nucleus of GS10578, with a velocity offset of $\approx 200 - 300$ km s^{-1} from GS10578. Notably, each of them has a Lyα luminosity comparable to that of GS10578 ($\approx 10^{42}$ erg s^{-1}). We also note that GS10578 lies $\sim$ 50 kpc (and $\sim$ 6000 km s^{-1}) from another Lyα halo discovered by Leclercq et al. (2017, see e.g. Fig. 9 in Perna et al. 2025). This suggests that GS10578 is embedded in a large-scale overdensity.

A previous analysis of MUSE rest-frame UV spectra suggested that the source labelled LAE2, despite its low stellar mass ($\log(M_\star/M_\odot) \approx 8.3 \pm 0.4$), is powered by an AGN based on UV-line ratio diagnostics (e.g. C IV/He II λ1640; Perna et al. 2025). LAE1 instead is only detected in Lyα, not in any other UV lines nor in imaging data from HST, JWST/NIRCam, and JWST/MIRI observations (Eisenstein et al. 2026; Rieke et al. 2023; Alberts et al. 2024). Confirming the AGN nature of LAE2 is particularly relevant in the broader context of black-hole growth in low-mass galaxies and the assembly of multi-AGN systems at high redshift, which present key constraints for hierarchical galaxy formation models and early SMBH seeding scenarios (e.g. Volonteri et al. 2022; Chen et al. 2025; Puerto-Sánchez et al. 2025; Scialpi et al. 2025). The nature of LAE1, instead, provides complementary insight into the ionisation and gas structure of the environment, as its Lyα-only detection may arise from resonant scattering or fluorescence powered by nearby ionising sources within the system (e.g. Cai et al. 2017). Taken together, LAE1 and LAE2 can thus trace distinct physical processes in the surroundings of GS10578, offering a unique opportunity to investigate how feedback, accretion, and satellite interactions shape the final stages of massive-galaxy assembly.

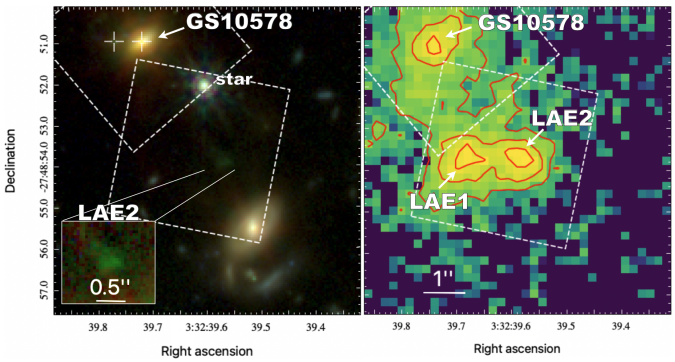

Fig. 1. Environmental context of GS10578 and its close emitters. *Left:* NIRCam three-colour composite image constructed from the F090W (blue), F200W (green), and F444W (red) filters. The main GS10578 galaxy is visible in the upper-left region, while the faint, clumpy [O III] emitter associated with LAE2 is detected near the field centre (see also the zoomed-in view in the inset). The two white crosses identify AGN-A (in GS10578) and AGN-B (in the close satellite). Right: VLT/MUSE narrow-band image obtained by integrating over the Lyα line (in the [–1000,+600] km s^{-1} range with respect to the systemic velocity of GS10578), revealing the extended nebula encompassing GS10578, LAE1, and LAE2 (contours at 3, 6, and 9σ, with $3\sigma = 6 \times 10^{-18}$ erg s^{-1} cm^{-2} arcsec^{-2}, estimated from the source-free region of the image). The footprints of the NIRSpec IFU observations from Cycle 1 (covering GS10578) and Cycle 3 (targeting LAE1 and LAE2) are overlaid in both panels. 1″ corresponds to 7.8 kpc at $z \sim 3$.

In this work, we present new, deep JWST/NIRSpec IFS observations specifically covering the rest-frame optical emission lines of LAE1 and LAE2: namely, Hβ, [O III] $\lambda\lambda$4960,5008, Hα, [N II] $\lambda\lambda$6550,6585, and [S II] $\lambda\lambda$6718,6732. These two satellites lie outside the NIRSpec IFS field of view (FOV) of the Cycle 1 observations used to characterise GS10578 (Fig. 1), and their optical line emission was not previously accessible. Our primary objectives were to robustly confirm the nature of LAE2 using established optical and UV diagnostic diagrams and to investigate its physical and kinematic properties in detail. We also used available multi-wavelength information to investigate the nature of LAE1. This paper is organised as follows. Section 2 describes the observations and data reduction procedures, Sect. 3 presents the data analysis, and Sect. 4 shows the ISM kinematic and physical properties inferred from emission-line analysis of NIRSpec IFS data. Finally, Sect. 5 discusses the implications of our findings, and Sect. 6 summarises our conclusions. Throughout, we adopted a Chabrier (2003) initial mass function (IMF, 0.1 – 100 $M_\odot$) and a flat ΛCDM cosmology with $H_0 = 70$ km s^{-1} Mpc^{-1}, $\Omega_\Lambda = 0.7$, and $\Omega_m = 0.3$.

2. Observations and data reduction

The NIRSpec IFS data analysed in this work cover LAE1 and LAE2 and were observed with the JWST/NIRSpec spectrograph in its IFS mode (Böker et al. 2022). Data were obtained as part of the NIRSpec IFS GTO programme 'Galaxy Assembly with

NIRSpec IFS' (GA-NIFS[1], e.g. Bertola et al. 2025; Jones et al. 2026; Lamperti et al. 2024; Trefoloni et al. 2025; Zamora et al. 2025) under the programme ID 4528 (P.I. Kate Isaak).

The IFS observations were taken with the grating/filter pair G235H/F170LP. This results in a data cube with spectral resolution of $R \sim 2700$ over the wavelength range 1.7–3.1 μm (Jakobsen et al. 2022). The observations were taken with the NRSIRS2 readout pattern (Rauscher et al. 2017) with 16 groups per integration and one integration per exposure, using a 12-point medium cycling dither pattern, resulting in a total exposure time of 3.9 hours, matching the one of Cycle 1 covering GS10578.

We downloaded raw data files from the Barbara A. Mikulski Archive for Space Telescopes (MAST) and subsequently processed them with the JWST Science Calibration pipeline (version 1.17.1) under the recommended Calibration Reference Data System (CRDS) context jwst_1322.pmap[2]. Some modifications to the pipeline allowed us to improve the data quality, and they are described in detail in Perna et al. (2023). Here, we summarise the main changes. First, we applied the 'calwebb_detector1' step of the pipeline to account for detector level correction. Before calibrating the count-rate images through the 'calwebb_spec2' module of the pipeline, we corrected them by subtracting the 1/f noise through a polynomial fitting. We identified and removed outliers directly in the calibrated 2D images, by applying an algorithm similar to 'lacosmic' (van Dokkum 2001), as implemented by D'Eugenio et al. (2024). The final data cube was created by combining the individual calibrated 2D exposures using the 'drizzle' weighting and obtaining a cube with a spaxel size of 0.05″.

The reduced MUSE data cube used in this work was retrieved from the ESO archive. The observations are part of the MUSE Ultra Deep Field (UDF) programme and correspond to the publicly released mosaic described in Bacon et al. (2017). The full dataset consists of a 3×3 mosaic, with individual pointings reaching a total exposure time of ~ 10 hours each. The publicly available data products have a spatial sampling of 0.2″ per pixel and a $\mathrm{FWHM_{PSF}} \approx 0.7''$. The astrometric alignment of the JWST and MUSE data was computed relatively to five bright stars detected in NIRCam images that were registered to Gaia DR2.

The overall environmental context of the GS10578 system is illustrated in Fig. 1. We used JWST/NIRCam imaging obtained in the wide filters F090W, F200W, and F444W (as retrieved from the Cosmic Dawn JWST Archive, from the JADES programme PID1180), to construct the three-colour composite image in the left panel. The GS10578 emission is clearly visible in the upper left region of the field, while the central part of the image reveals faint, multi-component [O III] line emission associated with LAE2 (see zoomed-in view in the inset); LAE1 remains undetected in NIRCam images. The right panel of Fig. 1 shows the corresponding VLT/MUSE map of the extended Lyα emission, which spatially resolves LAE1 and LAE2 relatively to the main system.

Both panels in Fig. 1 indicate the FOV of the NIRSpec IFS observations with dashed white boxes. The Cycle 1 data cover the GS10578 galaxy, whereas the new Cycle 3 observations presented in this work target LAE1 and LAE2.

[1] https://ga-nifs.github.io/
[2] https://jwst-crds.stsci.edu/display_build_contexts/

3. Data analysis

In this section we describe the method used to derive the emission-line properties of LAE1 and LAE2 by fitting the R2700 data. The method applies to both individual spaxel spectra and spatially integrated spectra.

As the continuum was not detected in the spectra, we did not model it. We fitted the most prominent gas emission lines by using the Levenberg-Marquardt least-squares fitting code CAPMPFIT (Cappellari 2017). In particular, we modelled the Hα, Hβ, and [O III] $\lambda\lambda$4960,5008 lines. The He II λ4687 line, [N II] $\lambda\lambda$6550,85 and [S II] $\lambda\lambda$6718,32 doublets were not detected in our data. We applied a simultaneous fitting procedure, so that all line features of a given kinematic component have the same velocity centroid and intrinsic velocity dispersion (e.g. Perna et al. 2020). Intrinsic velocity dispersions are obtained using the JWST/NIRSpec fiducial resolving power curves recorded here[3]. Moreover, the relative flux of the [O III] doublet components was fixed to 2.99 (Osterbrock & Ferland 2006). Each fit was performed with one and two Gaussian components. The final number of kinematic components used to model individual spectra was derived on the basis of the Bayesian information criterion (Schwarz 1978). For both integrated and spaxel-by-spaxel analysis a single Gaussian component is enough to reproduce the data.

4. Results

The LAE2 shows multiple line detections, while no rest-frame optical emission is detected from LAE1 in the NIRSpec IFS data. This non-detection holds for all tested extraction apertures, from compact to extended, and is consistent with its lack of a counterpart in the NIRCam imaging.

Integrated spectra of LAE2 were extracted using circular apertures of radii $r = 0.15''$ and $r = 0.5''$. The smaller aperture maximises the signal-to-noise ratio (S/N) in the emission lines and was used to study the ionisation conditions in the nuclear region of LAE2. The current data, however, did not allow us to precisely identify the nucleus of LAE2. The highest ionisation line detected, He II λ1640, was observed with MUSE at low spatial resolution, while the NIRCam continuum imaging is not sufficiently deep for a robust morphological classification (Fig. 1). We therefore adopted the peak of the [O III] λ5008 emission as a proxy for the nuclear position of this system. The larger aperture ($r = 0.5''$) captures the total emission from the system and enables a direct comparison with the Lyα flux measured from MUSE data, for which the spatial resolution is insufficient to resolve sub-kiloparsec scales within LAE2.

Figure 2 presents the nuclear spectrum of LAE2. Prominent [O III], Hα, and Hβ emission lines were detected, while He II, [N II], and [S II] remain undetected. No clear evidence for a broad-line region was found, although the modest S/N of the Hα line ($\mathrm{S/N} \lesssim 15$) did not allow us to exclude its possible presence. The best-fit single-Gaussian model is shown in red in Fig. 2 and yields a systemic redshift of $z = 3.06674 \pm 0.00005$. The integrated fluxes and kinematic properties derived from both apertures are summarised in Table 1. We note that the Balmer ratio is compatible with no extinction.

Figure 3 displays the spatial distributions of the Hα and [O III] fluxes, as well as the corresponding centroid velocity and

[3] https://jwst-docs.stsci.edu/jwst-near-infrared-spectrograph/nirspec-instrumentation/nirspec-dispersers-and-filters.

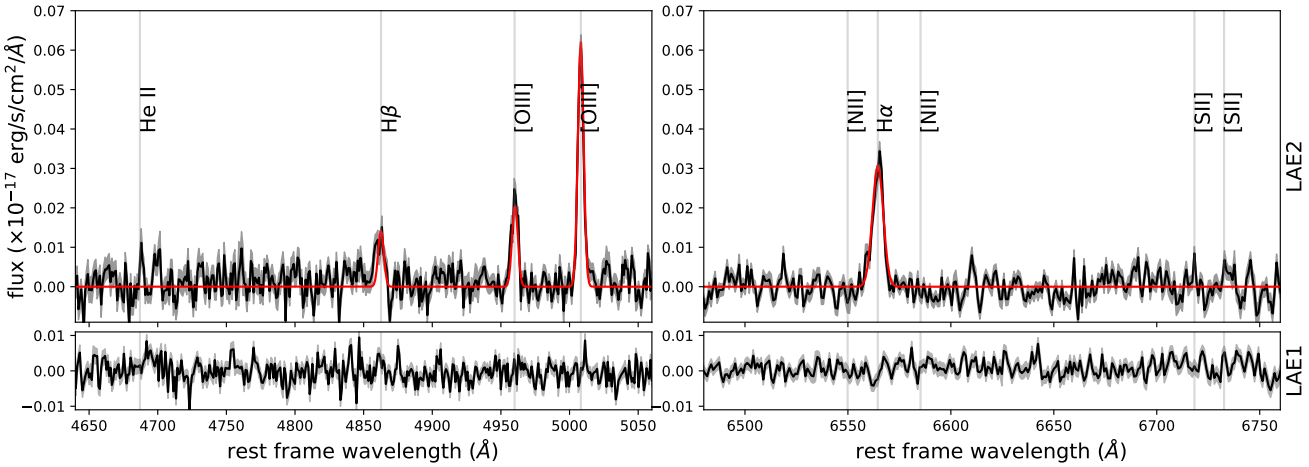

Fig. 2. Integrated NIRSpec spectra of LAE2 and LAE1 extracted within circular apertures of $r = 0.15''$. The main optical emission lines are labelled. Top panels: The spectrum of LAE2 (black curve) shows strong detections of Hβ, [O III]$\lambda\lambda$4960,5008, and Hα. The He IIλ4687, [N II], and [S II] lines are not detected above the 3σ noise level of the data. The red curve shows the best-fit model for LAE2. Bottom: The spectrum of LAE1 does not show any detectable emission features. The shaded regions indicate the 1σ uncertainties for both LAE2 (top) and LAE1 (bottom).

velocity-dispersion maps, obtained from spaxel-by-spaxel analysis. Both lines show extended, clumpy morphologies and irregular kinematics, consistent with the presence of multiple substructures already hinted at in the NIRCam F200W imaging.

4.1. Optical-line-ratio diagnostics

We investigated the dominant ionisation source for the emitting gas in LAE2 using the classical BPT diagram (Baldwin et al. 1981). Figure 4 (left) shows the [O III]/Hβ versus [N II]/Hα flux ratios measured from the nuclear ($r = 0.15''$) spectrum. For comparison, the BPT also displays other optical-line-ratio measurements from low-z SDSS galaxies (small grey points) and the demarcation lines used to separate galaxies and AGNs at $z \sim 0$.

Since the physical conditions of the ISM in galaxies at $z > 3$ differ substantially from the local population, both AGNs and star-forming galaxies tend to populate the same region of the BPT diagram when associated with low gas metallicities (e.g. Feltre et al. 2016; Nakajima & Maiolino 2022; Harikane et al. 2023; Übler et al. 2023; Maiolino et al. 2024), with low [N II]/Hα and high [O III]/Hβ, similar to those measured for LAE2. Therefore, additional diagnostics tailored to the early Universe have been proposed, several of which exploit the properties of He II λ4687 emission (e.g. Shirazi & Brinchmann 2012; Bär et al. 2017; Nakajima & Maiolino 2022; Tozzi et al. 2023). Figure 4 (right) shows LAE2 measurements on the He IIλ4687/Hβ versus [N II]/Hα diagram. In the rest-optical NIRSpec spectrum, both He IIλ4687 and [N II] are undetected, yielding an upper limit on both He II λ4687/Hβ and [N II]/Hα (large red circle in the figure). Taken alone, this diagram does not tightly constrain the ionisation mechanism, because the allowed region overlaps both the AGN and star-forming loci. However, additional information comes from the He IIλ1640 line detected in the MUSE rest-UV spectrum of LAE2. Because He IIλ1640 emission is known to be significantly more compact than Lyα and other UV lines such as C IV or C III] (e.g. Guo et al. 2020), it is reasonable to combine the He IIλ1640 flux measured with MUSE (despite its lower spatial resolution) with the Hβ flux extracted from our smallest NIRSpec aperture.

Using PYNEB (Luridiana et al. 2015) to convert the He IIλ1640 flux into the expected optical He II λ4687 flux taking advantage of their known recombination value He II λ1640/λ4687 = 6.47 (assuming an electron temperature of 10^4 K, an electron density $n_e = 100$ cm^{-3}, and no dust extinction), we obtained an estimated ratio of He II λ4687/Hβ = 0.16. This value represents a lower limit (red star in Fig. 4), since any dust attenuation preferentially suppresses the UV line and would increase the intrinsic ratio. Higher electron temperatures would also slightly modify the intrinsic recombination ratio (e.g. He IIλ1640/λ4687 = 7.35 at $T_e = 2 \times 10^4$ K, with negligible dependence on n_e), but this would translate into a change of $\sim 10\%$ in He IIλ4687/Hβ, without affecting our conclusions.

The combined UV–optical constraints therefore place He II λ4687/Hβ in a definite, AGN-only region of the diagnostic plane that is incompatible with pure stellar photoionisation. This provides strong evidence that LAE2 hosts an AGN, extending the MUSE-based indications reported by Perna et al. (2025, see their Fig. 12).

4.2. Lyα escape

Using hydrogen emission lines, it is possible to derive an escape fraction for Lyα under certain assumptions. Assuming Case B recombination and a dust-free environment, $n_e = 100$ cm^{-3} and $T_e = 10000$ K; the intrinsic Lyα/Hα ratio is 8.22 (Luridiana et al. 2015). Under these conditions, and neglecting the effects of resonant scattering (see below), the Lyα escape fraction f_{esc}(Lyα) can then be calculated as $f_{esc}(Ly\alpha) = L(Ly\alpha)/(8.22 \times L(H\alpha))$.

Using the MUSE Lyα flux measured from the best-fit spectral profile extracted within a circular aperture of $r = 0.5''$, matched to the NIRSpec extraction for Hα, we obtained $f_{esc}(Ly\alpha) = 0.15 \pm 0.03$ for LAE2. This value is consistent with previous measurements for Lyα-emitting galaxies at similar redshift (e.g. Hayes et al. 2011; Song et al. 2014). We note, however, that resonant scattering can substantially modify the intrinsic Lyα/Hα ratio by increasing the effective path length of Lyα photons and thus enhancing dust absorption, as well as by redistributing Lyα emission spatially and spectrally through multiple scatterings that can redirect photons out of the line of sight or allow them to escape through low-column-density channels. Therefore, we also applied the semi-empirical calibration by Sobral & Matthee (2019), f_{esc}(Lyα)

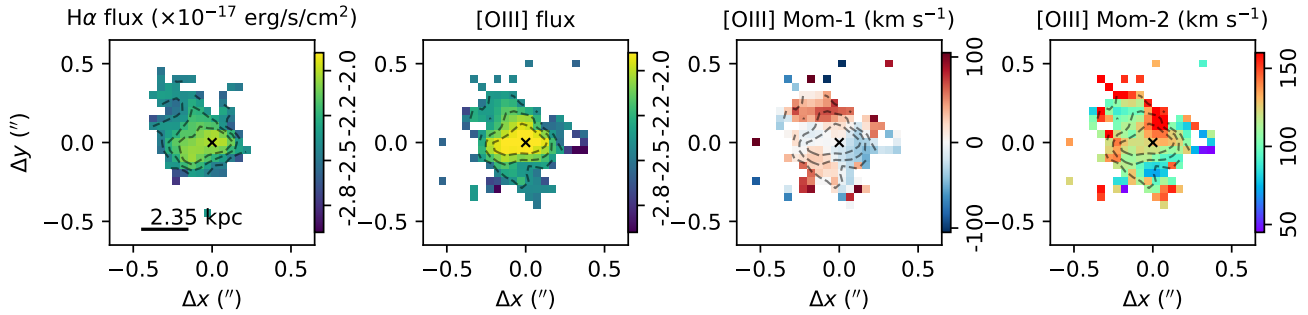

Fig. 3. Hα and [O III] flux distributions, along with the [O III] moment-1 (velocity) and moment-2 (velocity dispersion) maps of LAE2. The flux maps reveal the clumpy morphology of LAE2. The velocity map displays a velocity gradient along the south-east north-west direction in addition to a redshifted component in the northern part of the LAE2, possibly due to an additional component overlapping on the LOS. The contours in the first panel trace Hα emission (at 6, 9, and 12σ); those in the remaining panels trace [O III] emission (at 12, 20, and 30σ). All images are oriented north (up), with east to the left; fluxes are in log scale.

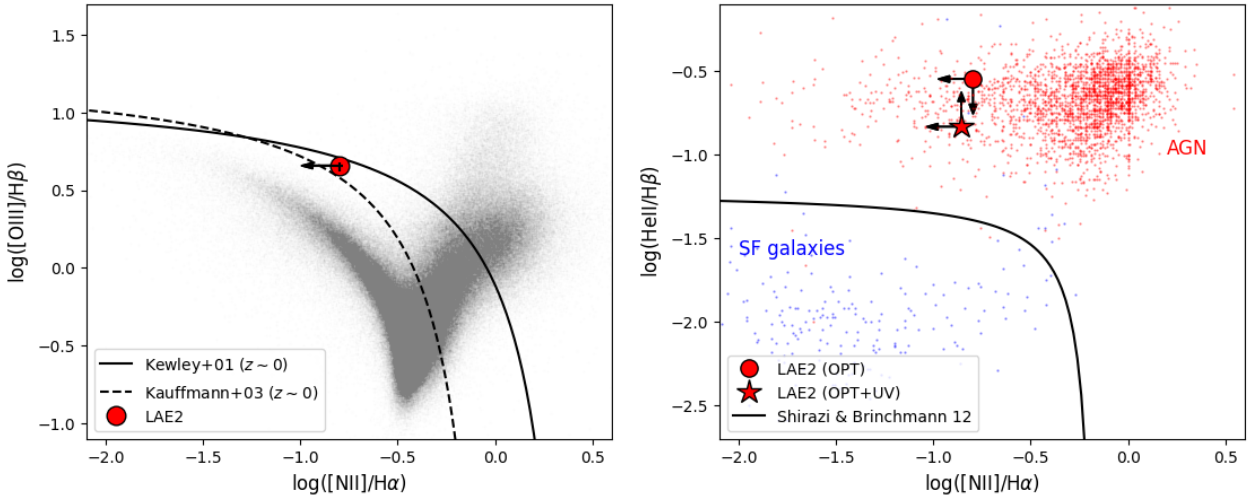

Fig. 4. BPT and He II diagnostic diagrams. Left: [N II]/Hα versus [O III]/Hβ for LAE2 (red symbol), compared with local SDSS galaxies (grey points; Abazajian et al. 2009). The solid (Kewley et al. 2001) and dashed (Kauffmann et al. 2003) curves mark the classical boundaries between star-forming galaxies (below the curves) and AGNs (above). Right: [N II]/Hα versus He II λ4687/Hβ for LAE2 (large red symbols), and local star-forming galaxies (blue) and AGNs (red) from Shirazi & Brinchmann (2012); the solid curve is used to separate star-forming galaxies (below the curve) and AGNs (above) according to Shirazi & Brinchmann (2012). The red circle indicates the 3σ upper limit on He II λ4687/Hβ (no He II λ4687 detection). The red star shows the corresponding lower limit obtained by assuming a fixed intrinsic ratio He II λ1640/He II λ4687 = 6.47, given that the UV line is detected but may be affected by extinction. Both symbols share the same [N II]/Hα ratio, but they are slightly offset horizontally for clarity.

= 0.0048×EW(Lyα)[Å^{-1}] ±0.05, to derive an independent estimate of the Lyα escape fraction, resulting in $f_{\rm esc}$(Lyα) = 0.27 ± 0.07, which is broadly consistent with the estimate obtained from Lyα/Hα. The EW is computed assuming a continuum level of 1.4×10^{-19} erg s^{-1} cm^{-2} Å^{-1} close to Lyα for LAE2, which was detected in HST imaging (from SED analysis; Appendix B; Perna et al. 2025) and resulted in an EW of 56 Å.

For LAE1, we can only place a lower limit on the Lyα equivalent width because no continuum is detected. Taking the continuum to be $\lesssim 1/2$ of that of LAE2 (consistent with the HST $\sim 6\sigma$ detection constraints of LAE2 and the non-detection of LAE1) and considering that LAE1 and LAE2 have similar Lyα fluxes (Table 1 and Fig. 5), we inferred EW(Lyα) $\gtrsim$ 140 Å for LAE1. This approaches the uppermost end of theoretical Lyα EWs expected for extremely young stellar populations (i.e. < 10 Myr, Charlot & Fall 1993). Applying the relation of Sobral & Matthee (2019) thus yielded a lower limit of $f_{\rm esc}$(Lyα) $\gtrsim$ 0.67. An independent constraint can be obtained using the upper limit on the Hα flux from the NIRSpec data, which implies $f_{\rm esc}$(Lyα) $\gtrsim$ 0.64 from the Lyα/Hα ratio. The consistency between these two independent estimates suggests that, under the assumption of in situ star formation, the Lyα escape fraction in LAE1 would be very high.

5. Discussion

The JWST/NIRSpec and VLT/MUSE observations of the GS10578-LAE1-LAE2 system provide a rare view of multiple Lyα-emitting components embedded within a common extended nebula at $z \sim 3$. The combination of deep NIRSpec and MUSE IFS data reveals markedly different physical conditions in the two satellites, LAE1 and LAE2, which are separated by a projected distance of $\sim$ 10 kpc. LAE2 shows high-ionisation UV lines, strong optical nebular emission, and bright Lyα and faint continuum emission, while LAE1 is detected exclusively in Lyα (with a similar luminosity to LAE2), with no continuum counterpart even in the deepest JWST imaging. Understanding the ori-

Table 1. Spatially integrated properties from the spectral analysis.

LAE2:	
RA: 3:32:39.5; DEC: –27:48:53.9	
Nuclear spectrum ($r = 0.15''$):	
z	$3.06674^{+0.00004}_{-0.00005}$
$\sigma_{\rm v,\ H\alpha}$	112^{+5}_{-2} km s^{-1}
log L([O III])/[erg s^{-1}]	41.44 ± 0.04
log L(Hα)/[erg s^{-1}]	41.24 ± 0.02
log L(He II 1640)/[erg s^{-1}]	40.82 ± 0.04
Hα/Hβ	$2.82^{+0.31}_{-0.25}$
E(B–V)	$0.01^{+0.10}_{-0.01}$
log([O III]/Hβ)	$0.65^{+0.04}_{-0.04}$
log([N II]/Hα)	< -0.79
log(He II 4687/Hβ)	< -0.51
log(He II 4687/Hβ)†	> -0.80
Integrated spectrum ($r = 0.50''$):	
log L(Lyα)/[erg s^{-1}]	41.81 ± 0.02
log L(Hα)/[erg s^{-1}]	41.72 ± 0.10
$\Delta v_{\rm Ly\alpha}$	105^{+5}_{-3} km s^{-1}
$\sigma_{\rm v,\ Ly\alpha}$	176 ± 3 km s^{-1}
$f_{\rm esc}$(Lyα)	0.15 – 0.27
EW(Lyα)	56 Å
LAE1:	
RA: 3:32:39.6; DEC: –27:48:53.8	
Integrated spectrum ($r = 0.50''$):	
log L(Lyα)/[erg s^{-1}]	41.90 ± 0.02
log L(Hα)/[erg s^{-1}]	< 41.17
log L(C III])/[erg s^{-1}]	< 40.53
$\Delta v_{\rm Ly\alpha}$	184^{+8}_{-4} km s^{-1}
$\sigma_{\rm v,\ Ly\alpha}$	220^{+7}_{-5} km s^{-1}
$f_{\rm esc}$(Lyα)	$\gtrsim 0.64$
EW(Lyα)	$\gtrsim 140$ Å

Notes. Lyα-emitter properties from JWST/NIRSpec (rest-frame optical) and VLT/MUSE (rest-frame UV). Colour excess measured from Hα/Hβ, assuming a Cardelli et al. (1989) dust-attenuation law. Hα and C III] upper limits for LAE1 obtained assuming a velocity dispersion of 112 and 210 km s^{-1}, respectively, corresponding to the values measured for the same lines in LAE2. LAE1 $\Delta v_{\rm Ly\alpha}$ relative to the LAE2 systemic zero velocity. Luminosities were not corrected for extinction, nor for aperture sizes. Equivalent widths are in the rest frame. All upper limits are quoted at the 3σ level.
†: assuming He II λ1640/λ4687 = 6.47; see Sect. 4.

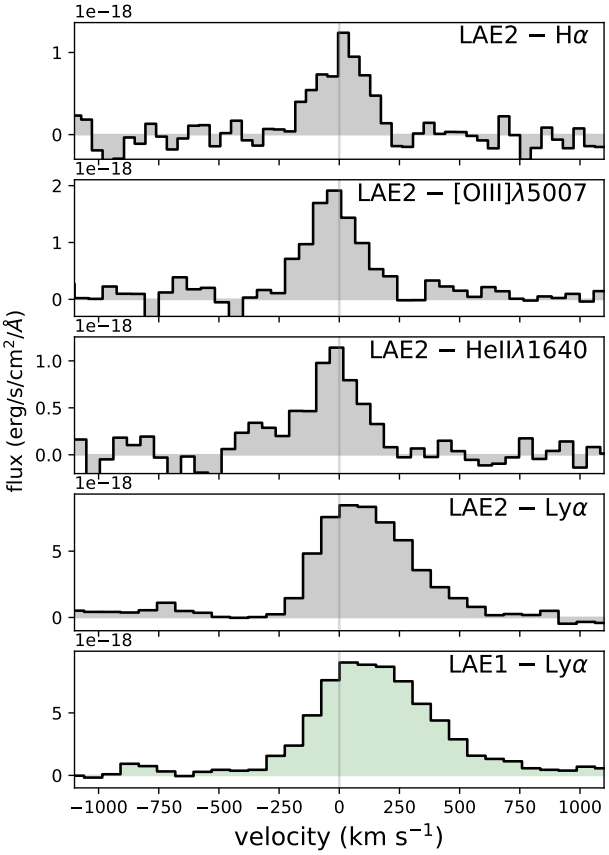

Fig. 5. Emission-line profiles of LAE2 (grey) and LAE1 (green) in velocity space. Lyα and He II lines from the MUSE spectrum and [O III] and Hα from NIRSpec IFS are both integrated over an aperture of $r = 0.5''$. The vertical line indicates the systemic velocity ($v = 0$) of LAE2.

gin of the ionising radiation and the mechanisms powering the Lyα emission in these components is essential for reconstructing the physical state of the gas within the system. In the following subsections, we separately examine the nature of LAE2, whose spectroscopic properties point to AGN-driven ionisation, and LAE1, whose bright but isolated Lyα emission raises the question of whether it is powered by scattering, fluorescence, or in situ star formation.

5.1. The nature of LAE2

The LAE2 system displays an irregular morphology in rest-frame optical emission lines, extending over a few kiloparsecs, with no clear evidence of ordered rotation in its velocity field (Fig. 3). This source remains unresolved in the lower angular-resolution MUSE data (Appendix A). Rest-frame UV and optical integrated spectra (from MUSE and NIRSpec, respectively) show that He II λ1640, [O III] λ5008, and Hα share the same systemic velocity (Fig. 5); this indicates that the UV and optical ionised gas components trace a common kinematic structure. The presence of high-ionisation UV transitions and the line ratios inferred from deep MUSE data both point to a hard ionising spectrum (Perna et al. 2025). In this work, by combining NIRSpec IFS and MUSE data, we applied both classical and high-redshift optical diagnostics (Fig. 4); although LAE2 lies outside the regime where BPT diagram is reliable for low-mass and low-metallicity systems, the He II λ4687 diagnostic robustly places it in the AGN-ionised regime.

The Hα velocity dispersion reaches values of $\approx$ 100 km s^{-1} (Fig. 3), which is unusually high for a low-mass, low-SFR system such as LAE2. For comparison, massive main-sequence galaxies at similar redshifts typically exhibit velocity dispersions of $\sigma \approx 50$ km s^{-1}, albeit with substantial scatter (e.g. Übler et al. 2019). Dispersions of $\sim$ 100 km s^{-1} are instead observed in systems undergoing extreme star formation episodes (see e.g. Fig. 7 in Perna et al. 2022), well above the star formation rates inferred for LAE2 from its hydrogen recombination lines (Sect. 5.3). This elevated velocity dispersion is therefore also consistent with the presence of AGN-driven feedback acting on the ionised gas. Alternatively, part of the observed velocity dispersion may arise from the superposition of multiple unresolved clumps (Figs. 1 and 3) and their mutual gravitational interactions.

The Lyα spectral profile of LAE2 exhibits a dominant red wing with a small offset from the systemic velocity, $\Delta v_{\rm Ly\alpha}$ =

105^{+5}_{-3} km s^{-1} (Fig. 5). Radiative-transfer models from Verhamme et al. (2015) provide a useful interpretative framework for this profile. They explored two idealised cases of galaxies leaking Lyman-continuum radiation: (1) homogeneous, spherically expanding shells with extremely low H I column densities ($N_{HI} \lesssim 10^{18}$ cm^{-2}), which produce asymmetric, redshifted profiles with velocity peaks of $\lesssim 150$ km s^{-1} from systemic, or double-peaked profiles with peak separations of $\lesssim 300$ km s^{-1}; and (2) clumpy shells with incomplete neutral-gas covering, producing profiles peaked very close to the systemic velocity. The Lyα profile of LAE2 closely resembles the first class of models, suggesting an ISM dominated by a relatively homogeneous, low-column-density neutral gas component in expansion. This configuration naturally arises when the ISM is exposed to a hard ionising spectrum capable of reducing the effective neutral-gas opacity, which is also consistent with the presence of an AGN (see also e.g. Yang et al. 2014).

In Appendix B, we present a spectral energy distribution (SED) analysis of LAE2 that extends the work of Perna et al. (2025, and Circosta et al., in prep.) by explicitly including a potential AGN contribution in the modelling. Allowing for a composite stellar+AGN SED, we find that the photometry of LAE2 is well reproduced with an AGN fractional contribution of $f_{AGN} = 0.4 \pm 0.2$. The inclusion of an AGN component leads to a slightly lower inferred stellar mass, $\log(M_\star/M_\odot) = 7.78^{+0.18}_{-0.32}$, compared to purely stellar models. The best-fit solution favours a young stellar population with an age of ~ 415 Myr (corresponding to a formation redshift of $z \sim 3.5$–4) and a modest, ongoing star formation rate, SFR ≈ 0.13 M$_\odot$ yr^{-1}, which is in good agreement with the constraints derived from hydrogen recombination lines (Sect. 5.3).

5.2. The nature of LAE1

Spatially offset Lyα emission with little or no continuum counterpart has been reported in a number of deep, narrow-band and IFS studies, and is commonly interpreted as either fluorescence of gas illuminated by an external source, scattering of Lyα photons from a nearby galaxy, or cooling radiation from accreting gas (e.g. Villar-Martin et al. 1996; Bunker et al. 2000; Nilsson et al. 2006; Geach et al. 2009; Cantalupo et al. 2012; Vanzella et al. 2017).

A number of published systems show qualitative similarities to the LAE1–LAE2 pair. For instance, Vanzella et al. (2017) used MUSE observations of a strongly lensed system at $z \simeq 3.3$ to identify a compact Lyα emitter located ~ 2 kpc from a bright star-forming galaxy. The Lyα line in this offset component is narrow (FWHM $\lesssim 100$ km s^{-1}) and lies at the same systemic redshift as the main galaxy, consistent with fluorescence from gas externally ionised by radiation escaping from the central source. A faint continuum counterpart is marginally detected in the HST imaging, suggesting a low-mass or gas-dominated clump illuminated by the nearby galaxy. More recently, Zarattini et al. (2025) reported the discovery of a Lyα knot close to a galaxy at $z \simeq 3.5$, characterised by extended (5–8 kpc) Lyα emission at a projected distance of 6 kpc. In this case, a faint UV continuum is detected in the knot, indicating that in situ star formation may contribute to the observed emission, although the authors also discussed the possibility that the structure traces an ionised cone of radiation escaping from the main galaxy. No spectroscopic information is available for this system, however. While morphologically reminiscent of our LAE1–LAE2 pair, separated by a projected distance of ~ 10 kpc, these examples differ spectroscopically. LAE1 shows a broad and asymmetric Lyα profile and remains undetected in the UV, unlike the narrow, symmetric, or continuum-detected knots in the systems mentioned above. Moreover, a fluorescence origin for LAE1 requires an external source bright enough to power a Lyα luminosity of $\sim 10^{42}$ erg s^{-1}. Neither LAE2 nor GS10578 meet this requirement: (a) the X-ray AGN in GS10578 has an ionising luminosity orders of magnitude too low (Perna et al. 2025); (b) GS10578 is quiescent, with its major star formation episode ending ~ 0.5 Gyr ago; (c) LAE2 has a Lyα luminosity comparable to LAE1, and thus it cannot power LAE1 through fluorescence at a projected distance of 8 kpc. Moreover, if LAE1 were purely fluorescent, Hα emission would be detectable at a 2σ confidence level within an aperture of $r = 0.5''$, assuming a ratio of Lyα/Hα = 8.22 (or $> 2\sigma$ in smaller apertures). Thus, a fluorescence interpretation is strongly disfavoured.

Large Lyα blobs (LABs) at high redshift often contain subcomponents or 'knots' without detectable continuum emission (e.g. Herenz et al. 2020; Rahna et al. 2025; Solimano et al. 2025). Some of these knots show broad Lyα profiled ($\sigma \approx 200$ km s^{-1}) and appear disconnected from known galaxies (e.g. Fig. 11 of Jiménez-Andrade et al. 2023). However, these LAB systems are usually characterised by a Lyα nebula extending over $\gtrsim 100$ kpc, a global Lyα luminosity of $> 10^{43.5}$ erg s^{-1}, and are associated with radio galaxies. Our system GS10578-LAE1–LAE2 is less extended (~ 50 kpc) and more balanced in luminosity between components, with L(Lyα) $\approx 10^{42}$ erg s^{-1} each, suggesting a different physical configuration than a classical LAB.

LAE1 exhibits a broad and asymmetric Lyα profile, no detectable continuum counterpart, and a location embedded within a disturbed Lyα halo connecting GS10578, LAE2, and LAE1. These features are most naturally explained if LAE1 is dominated by resonant scattering of Lyα photons produced in LAE2. A roughly similar configuration has been reported in lensed systems at $z = 4$ by Bunker et al. (2000), in which Lyα emission is significantly more extended than the UV continuum and shaped by radiative transfer through neutral gas.

The similarity between the Lyα line profiles of LAE1 and LAE2 suggests that both sources are viewed through a common, extended structure of neutral hydrogen, likely an expanding or turbulent screen in the circumgalactic medium that covers both objects. The interaction with the massive GS10578 galaxy may have enhanced the turbulence and bulk motions of this medium, increasing the efficiency of resonant scattering and shaping the emergent Lyα profiles. This is supported by Fig. 6, which shows spatially varying Lyα profiles over an $\sim 40\times40$ kpc^2 region; diffuse, perturbed Lyα emission is visible between the three emitters, with a double-peaked profile near GS10578 (peak separation ~600 km s^{-1}) and redshifted profile near LAE1 and LAE2. Within this framework, the markedly different Lyα escape fractions and Lyα/Hα ratios observed in LAE1 and LAE2 (Table 1) can be understood if LAE2 hosts an AGN that provides a local source of ionisation, while LAE1 lacks in situ star formation and primarily reprocesses Lyα photons propagating through the shared neutral medium.

5.3. A possible alternative scenario for LAE1

Although the observational evidence favours a scattering-dominated origin for LAE1, it is worth considering whether LAE1 could instead host its own ionising source, and hence whether it is a faint galaxy whose stellar continuum remains undetected even in deep JWST data. To the first order, the SFR inferred from recombination lines falls in the regime of low-mass galaxies. We derived an estimate for the SFR from the Lyα line,

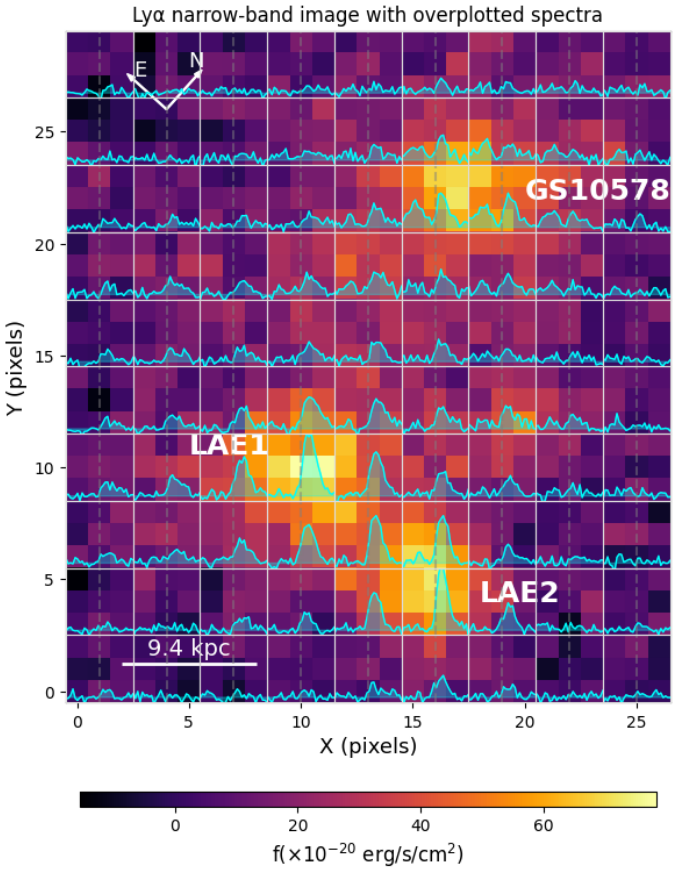

Fig. 6. Lyα narrow-band image obtained by integrating the MUSE cube over the [–900, +600] km s^{-1} velocity range around the Lyα line at the systemic redshift of the GS10578 galaxy. The background image shows the spatial distribution of the Lyα flux, with a compass in the top left corner indicating the north and east directions and a 1.2″ scale bar in the bottom left. Superimposed are the spectra extracted from 3 × 3 spaxel boxes at the positions marked in the image. All spectra are displayed with the same axis limits, spanning −1100 to +1000 km s^{-1} and (−7 to 88)×10^{-20} erg s^{-1} cm^{-2} Å^{-1} along the vertical axis. The dashed vertical line indicates the systemic velocity (v = 0) of GS10578 (blueshifted by 200 km s^{-1} from LAE2).

starting from the better calibrated Hα star formation indicator (Kennicutt & Evans 2012) and assuming Case-B recombination: SFR(Lyα) [M$_\odot$ yr^{-1}] = 5 × 10^{-43} L(Lyα) [erg s^{-1}]. We obtained SFR(LAE1) = 0.4 M$_\odot$ yr^{-1}. According to the star-forming main sequence at this redshift (Speagle et al. 2014), such SFRs correspond to stellar masses of the order of $\lesssim 10^8$ M$_\odot$. Thus, if LAE1 hosts in situ star formation, it would correspond to a very low-mass galaxy. In Appendix B, we detail how we used the non-detections in the available HST and JWST imaging to perform a tentative SED analysis and place an upper limit on the stellar mass of LAE1 of M$_\star \lesssim 10^{6.5}$ M$_\odot$. This limit is more than an order of magnitude lower than the stellar mass inferred for LAE2 (M$_\star \approx 10^8$ M$_\odot$), is difficult to reconcile with the SFR implied by the Lyα luminosity, and would require very high specific star formation if the Lyα emission were powered by in situ star formation.

Given that the SED constraints alone cannot fully rule out a faint stellar component, we next turned to rest-frame UV emission-line diagnostics to further test the possibility of in situ star formation in LAE1. A powerful diagnostic for faint star-forming galaxies at $z \sim 3$ is the C III] $\lambda\lambda$1907, 1909 doublet, which is typically the brightest UV metal line in this population (e.g. Shapley et al. 2003). If LAE1 were powered by its own stars, the empirical correlation between Lyα and C III] equivalent widths (Llerena et al. 2022) would provide an estimate of the expected C III] strength. Given the lower limit EW(Lyα) > 140 Å, the relation predicts EW(C III]) $\gtrsim$ 16 Å.

Assuming LAE1 has an intrinsic UV slope of $\beta = -2.62$ (Boquien et al. 2022) and negligible dust, the continuum near C III] scales as

$$f_{\mathrm{con,\,CIII]}} = \left(\frac{\lambda_{\mathrm{CIII]}}{\lambda_{\mathrm{Ly}\alpha}}\right)^{\beta} f_{\mathrm{con,\,Ly}\alpha} \approx 0.3\, f_{\mathrm{con,\,Ly}\alpha}, \quad (1)$$

where $f_{\mathrm{con,Ly}\alpha}$ is the continuum near Lyα. Under these assumptions, the expected C III] line luminosity can be obtained from

$$\frac{\mathrm{EW(Ly}\alpha)}{\mathrm{EW(CIII])}} = \frac{L(\mathrm{Ly}\alpha)/f_{\mathrm{con,Ly}\alpha}}{L(\mathrm{CIII])}/f_{\mathrm{con,CIII]}} = 0.3 \times \frac{L(\mathrm{Ly}\alpha)}{L(\mathrm{CIII])}}. \quad (2)$$

To the first order, we assumed an EW(Lyα) = 140 Å (i.e. similar to the measured lower limit) and took advantage of the known correlation between EW(Lyα) and EW(C III]) for star-forming galaxies at $z \sim 3$ from Llerena et al. (2022, their Eq. 1) to obtain an estimate of EW(C III]) = 16 Å. By doing so, the previous equation can be used to obtain an estimate of C III] luminosity, as L(C III]) = 0.03 × L(Lyα) = $10^{40.43}$ erg s^{-1}.

Given the MUSE noise level near C III] of 7 × 10^{-20} erg s^{-1} cm^{-2} Å^{-1} and assuming a velocity dispersion of 120 km s^{-1} (as for the detected C III] in LAE2), the 3σ upper limit is L(C III]) = $10^{40.53}$ erg s^{-1}. Therefore, an extremely low-mass stellar population cannot yet be firmly excluded. However, we note that if LAE1 were an independent galaxy with its own ionising source, one would expect its Lyα profile to reflect its internal ISM conditions (gas kinematics, column density, outflows) and therefore would differ from that of LAE2. In contrast, the two profiles share a similar asymmetric shape (Figs. 5 and 6). This behaviour favours a connection between the two Lyα-emitters.

6. Conclusions

We present new JWST/NIRSpec IFS observations of the environment of the massive quiescent galaxy GS10578 at z = 3.064, targeting two nearby Lyα emitters (LAE1 and LAE2) previously identified in deep VLT/MUSE data. Combined with the MUSE cube and ancillary JWST/NIRCam imaging, our analysis provides a spatially resolved view of ionised gas, kinematics, and AGN activity within ∼ 30 kpc of one of the earliest quenched galaxies known at high redshift. Our main conclusions are listed below.

– Our NIRSpec data confirm the presence of an active nucleus in LAE2, adding to the AGN in GS10578 itself and to the previously identified obscured nucleus in the nearby satellite (both outside the FOV of the NIRSpec data discussed here; Perna et al. 2025). This system therefore hosts three AGNs within ∼ 30 kpc, making it one of the most compact multi-AGN environments known at $z > 3$. This configuration provides additional, clear evidence of accelerated black-hole growth in dense environments surrounding massive quenched galaxies.

– LAE1 shows bright Lyα emission with no detected continuum counterpart in either NIRCam or MIRI imaging. Its broad, asymmetric Lyα profile, lack of Balmer and metal lines, and spatial correspondence with the Lyα halo around GS10578 favour an interpretation in which LAE1 traces scattered emission from LAE2, rather than an independent galaxy. A fluorescence scenario would require ionising luminosities higher than permitted by the AGN in the LAE2 system. A low-mass ($\lesssim 10^{6.5}$ M$_\odot$) stellar population in LAE1 cannot be firmly excluded, but the fact that the Lyα profiles in LAE1 and LAE2 are very similar favours a connection between the two. In particular, an expanding or turbulent screen in the circumgalactic medium that covers both objects could shape their emergent Lyα emission.

The environment of GS10578 is a site of ongoing gas accretion and black-hole growth. Despite GS10578 being fully quenched for ~ 0.5 Gyr, its surroundings host gas-rich satellites, extended Lyα nebula, and multiple AGNs. This suggests that massive quenched galaxies at early times can reside in dynamically complex and gas-rich environments where SMBH fuelling continues independently of the massive galaxy's star formation history.

Overall, the GS10578-LAE1-LAE2 system highlights the power of combining JWST IFS data with deep MUSE spectroscopy to dissect the interplay of AGN activity, gas accretion, and galaxy evolution at $z > 3$. A possible broader context for our system is provided by the growing number of studies reporting multiple AGNs associated with large Lyα nebulae in protocluster environments at $z \sim 2$–3. Multiple AGNs have been identified in these overdense regions, including the ones associated with the Slug, Fabulous, and J0819 nebulae (Traina et al. 2025), as well as MQN01, the Spiderweb system, SSA22 (Travascio et al. 2025), and the BOSS1441 structure (Wu et al. 2025). In these cases, however, the active galaxies are typically distributed over scales of hundreds of kiloparsecs up to a few megaparsecs, as detected in X-ray observations, tracing large-scale structures or protocluster environments rather than compact galaxy associations. The only partial exception is for the MQN01 system, where two faint AGNs are located at projected separations of $\sim$ 20 kpc from each other and $\sim$ 70 kpc from a luminous QSO (see Fig. A.1 of Travascio et al. 2025). By contrast, the components of the GS10578-LAE1-LAE2 system are confined within $\lesssim$ 30 kpc, placing them on substantially smaller physical scales. Future observations will be essential to determine how common such compact multi-AGN configurations are, including within known overdense regions that still lack dedicated rest-frame UV-optical IFS observations—which are key to identifying faint AGNs—and to establish their role in shaping the early growth of massive galaxies and their central SMBHs.

Acknowledgements. We thank the anonymous referees for their constructive feedback that helped to improve the quality of this work. We thank Luis Colina, Luca Costantin, Manuel Solimano, Lorenzo Ulivi, Eros Vanzella, and Cristian Vignali for valuable discussions. MP, SA, BRP, and PPG acknowledge support from the research projects PID2021-127718NB-I00, PID2024-159902NA-I00, PID2024-158856NA-I00, and RYC2023-044853-I of the Spanish Ministry of Science and Innovation/State Agency of Research (MCIN/AEI/10.13039/501100011033) and FSE+. IL acknowledges support from PRIN-MUR project "PROMETEUS" financed by the European Union - Next Generation EU, Mission 4 Component 1 CUP B53D23004750006. RM acknowledges support by the Science and Technology Facilities Council (STFC), by the ERC Advanced Grant 695671 "QUENCH", and by the UKRI Frontier Research grant RISEandFALL; RM is further supported by a research professorship from the Royal Society. AJB acknowledges funding from the "First Galaxies" Advanced Grant from the European Research Council (ERC) under the European Union's Horizon 2020 research and innovation programme (Grant agreement No. 789056). SC and GV acknowledge support by European Union's HE ERC Starting Grant No. 101040227 - WINGS. MP, GC and EB acknowledge the support of the INAF Large Grant 2022 "The metal circle: a new sharp view of the baryon cycle up to Cosmic Dawn with the latest generation IFU facilities". GC and EB also acknowledge the INAF GO grant "A JWST/MIRI MIRACLE: Mid-IR Activity of Circumnuclear Line Emission". EB acknowledges funding through the INAF "Ricerca Fondamentale 2024" programme (mini-grant 1.05.24.07.01). HÜ acknowledges funding by the European Union (ERC APEX, 101164796). Views and opinions expressed are however those of the authors only and do not necessarily reflect those of the European Union or the European Research Council Executive Agency. Neither the European Union nor the granting authority can be held responsible for them. MVM research has been funded by grant Nr. PID2021-124665NB-I00 by the Spanish Ministry of Science and Innovation/State Agency of Research MCIN/AEI/ 10.13039/501100011033 and by "ERDF A way of making Europe".

References

Abazajian, K. N., Adelman-McCarthy, J. K., Agüeros, M. A., et al. 2009, ApJS, 182, 543
Alberts, S., Lyu, J., Shivaei, I., et al. 2024, ApJ, 976, 224
Bacon, R., Conseil, S., Mary, D., et al. 2017, A&A, 608, A1
Baker, W. M., Lim, S., D'Eugenio, F., et al. 2025, MNRAS, 539, 557
Baldwin, J. A., Phillips, M. M., & Terlevich, R. 1981, PASP, 93, 5
Bär, R. E., Weigel, A. K., Sartori, L. F., et al. 2017, MNRAS, 466, 2879
Bertola, E., Cresci, G., Venturi, G., et al. 2025, A&A, 699, A220
Bluck, A. F. L., Maiolino, R., Brownson, S., et al. 2022, A&A, 659, A160
Böker, T., Arribas, S., Lützgendorf, N., et al. 2022, A&A, 661, A82
Boquien, M., Buat, V., Burgarella, D., et al. 2022, A&A, 663, A50
Boquien, M., Burgarella, D., Roehlly, Y., et al. 2019, A&A, 622, A103
Boylan-Kolchin, M. 2023, Nature Astronomy, 7, 731
Bruzual, G. & Charlot, S. 2003, MNRAS, 344, 1000
Bunker, A. J., Moustakas, L. A., & Davis, M. 2000, ApJ, 531, 95
Cai, Z., Fan, X., Yang, Y., et al. 2017, ApJ, 837, 71
Calzetti, D., Armus, L., Bohlin, R. C., et al. 2000, ApJ, 533, 682
Cantalupo, S., Lilly, S. J., & Haehnelt, M. G. 2012, MNRAS, 425, 1992
Cappellari, M. 2017, MNRAS, 466, 798
Cardelli, J. A., Clayton, G. C., & Mathis, J. S. 1989, ApJ, 345, 245
Carnall, A. C., McLeod, D. J., McLure, R. J., et al. 2023, MNRAS, 520, 3974
Chabrier, G. 2003, PASP, 115, 763
Charlot, S. & Fall, S. M. 1993, ApJ, 415, 580
Chen, N., Zhou, Y., Dadiani, E., et al. 2025, arXiv e-prints, arXiv:2512.16844
Croton, D. J., Springel, V., White, S. D. M., et al. 2006, MNRAS, 365, 11
de Graaff, A., Setton, D. J., Brammer, G., et al. 2025, Nature Astronomy, 9, 280
D'Eugenio, F., Pérez-González, P. G., Maiolino, R., et al. 2024, Nature Astronomy, 8, 1443
Eisenstein, D. J., Johnson, B. D., Robertson, B., et al. 2025, ApJS, 281, 50
Eisenstein, D. J., Willott, C., Alberts, S., et al. 2026, ApJS, 283, 6
Feltre, A., Charlot, S., & Gutkin, J. 2016, MNRAS, 456, 3354
Fritz, J., Franceschini, A., & Hatziminaoglou, E. 2006, MNRAS, 366, 767
Geach, J. E., Alexander, D. M., Lehmer, B. D., et al. 2009, ApJ, 700, 1
Glazebrook, K., Nanayakkara, T., Schreiber, C., et al. 2024, Nature, 628, 277
Glazebrook, K., Schreiber, C., Labbé, I., et al. 2017, Nature, 544, 71
Guo, Y., Maiolino, R., Jiang, L., et al. 2020, ApJ, 898, 26
Harikane, Y., Zhang, Y., Nakajima, K., et al. 2023, ApJ, 959, 39
Hayes, M., Schaerer, D., Östlin, G., et al. 2011, ApJ, 730, 8
Herenz, E. C., Hayes, M., & Scarlata, C. 2020, A&A, 642, A55
Jakobsen, P., Ferruit, P., de Oliveira, C. A., et al. 2022, A&A, 661, A80
Jiménez-Andrade, E. F., Cantalupo, S., Magnelli, B., et al. 2023, MNRAS, 521, 2326
Jones, G. C., Bowler, R. A. A., Bunker, A. J., et al. 2026, MNRAS, 547, stag336
Kauffmann, G., Heckman, T. M., Tremonti, C., et al. 2003, MNRAS, 346, 1055
Kennicutt, R. C. & Evans, N. J. 2012, ARA&A, 50, 531
Kewley, L. J., Dopita, M. A., Sutherland, R. S., Heisler, C. A., & Trevena, J. 2001, ApJ, 556, 121
King, A. & Pounds, K. 2015, ARA&A, 53, 115
Lamperti, I., Arribas, S., Perna, M., et al. 2024, A&A, 691, A153
Leclercq, F., Bacon, R., Wisotzki, L., et al. 2017, A&A, 608, A8
Llerena, M., Amorín, R., Cullen, F., et al. 2022, A&A, 659, A16
Luridiana, V., Morisset, C., & Shaw, R. A. 2015, A&A, 573, A42
Lyu, J., Alberts, S., Rieke, G. H., & Rujopakarn, W. 2022, ApJ, 941, 191
Maiolino, R., Scholtz, J., Curtis-Lake, E., et al. 2024, A&A, 691, A145
McConachie, I., Antwi-Danso, J., Chang, W., et al. 2025, submitted to ApJ, arXiv e-prints, arXiv:2508.05752
Nakajima, K. & Maiolino, R. 2022, MNRAS, 513, 5134
Nilsson, K. K., Fynbo, J. P. U., Møller, P., Sommer-Larsen, J., & Ledoux, C. 2006, A&A, 452, L23
Osterbrock, D. E. & Ferland, G. J. 2006, Astrophysics of gaseous nebulae and active galactic nuclei (University Science Books)

Pascalau, R. G., D'Eugenio, F., Tacchella, S., et al. 2026, MNRAS, 547, stag210
Pérez-González, P. G., D'Eugenio, F., Rodríguez del Pino, B., et al. 2025, Nature Astronomy, 9, 1240
Perna, M., Arribas, S., Catalán-Torrecilla, C., et al. 2020, A&A, 643, A139
Perna, M., Arribas, S., Colina, L., et al. 2022, A&A, 662, A94
Perna, M., Arribas, S., Lamperti, I., et al. 2025, A&A, 696, A59
Perna, M., Arribas, S., Marshall, M., et al. 2023, A&A, 679, A89
Puerto-Sánchez, C., Habouzit, M., Volonteri, M., et al. 2025, MNRAS, 536, 3016
Rahna, P. T., Akhlaghi, M., Fernãndez-Ontiveros, J. A., et al. 2025, A&A, 703, L20
Rauscher, B. J., Arendt, R. G., Fixsen, D. J., et al. 2017, PASP, 129, 105003
Rieke, M. J., Robertson, B., Tacchella, S., et al. 2023, ApJS, 269, 16
Schartmann, M., Meisenheimer, K., Camenzind, M., Wolf, S., & Henning, T. 2005, A&A, 437, 861
Scholtz, J., D'Eugenio, F., Maiolino, R., et al. 2026, Nature Astronomy, 10, 431
Schwarz, U. J. 1978, A&A, 65, 345
Scialpi, M., Mannucci, F., D'Amato, Q., et al. 2025, A&A in press, arXiv e-prints, arXiv:2512.11960
Shapley, A. E., Steidel, C. C., Pettini, M., & Adelberger, K. L. 2003, ApJ, 588, 65
Shirazi, M. & Brinchmann, J. 2012, MNRAS, 421, 1043
Sobral, D. & Matthee, J. 2019, A&A, 623, A157
Solimano, M., González-López, J., Aravena, M., et al. 2025, A&A, 693, A70
Song, M., Finkelstein, S. L., Gebhardt, K., et al. 2014, ApJ, 791, 3
Speagle, J. S., Steinhardt, C. L., Capak, P. L., & Silverman, J. D. 2014, ApJS, 214, 15
Tozzi, G., Maiolino, R., Cresci, G., et al. 2023, MNRAS, 521, 1264
Traina, A., Vito, F., Arrigoni-Battaia, F., et al. 2025, A&A, 701, A158
Travascio, A., Cantalupo, S., Tozzi, P., et al. 2025, A&A, 694, A165
Trefoloni, B., Carniani, S., Bertola, E., et al. 2025, subm. to A&A, arXiv e-prints, arXiv:2509.07064
Übler, H., Genzel, R., Wisnioski, E., et al. 2019, ApJ, 880, 48
Übler, H., Maiolino, R., Curtis-Lake, E., et al. 2023, A&A, 677, A145
Valentino, F., Brammer, G., Gould, K. M. L., et al. 2023, ApJ, 947, 20
van Dokkum, P. G. 2001, PASP, 113, 1420
Vanzella, E., Castellano, M., Meneghetti, M., et al. 2017, ApJ, 842, 47
Venturi, G., Carniani, S., Bertola, E., et al. 2025, subm. to A&A, arXiv e-prints, arXiv:2512.09996
Verhamme, A., Orlitová, I., Schaerer, D., & Hayes, M. 2015, A&A, 578, A7
Villar-Martin, M., Binette, L., & Fosbury, R. A. E. 1996, A&A, 312, 751
Volonteri, M., Pfister, H., Beckmann, R., et al. 2022, MNRAS, 514, 640
Weibel, A., de Graaff, A., Setton, D. J., et al. 2025, ApJ, 983, 11
Wu, J., Dou, L., Cai, Z., et al. 2025, ApJ, 991, 183
Xie, L., De Lucia, G., Fontanot, F., et al. 2024, ApJ, 966, L2
Yang, Y., Zabludoff, A., Jahnke, K., & Davé, R. 2014, ApJ, 793, 114
Zamora, S., Venturi, G., Carniani, S., et al. 2025, A&A, 702, A102
Zarattini, S., Rodríguez-Espinosa, J. M., Muñoz-Tuñón, C., Mas-Hesse, J. M., & Arrabal Haro, P. 2025, A&A, 693, A133
Zinger, E., Pillepich, A., Nelson, D., et al. 2020, MNRAS, 499, 768

Appendix A: Lyα flux distribution of LAE1 and LAE2

To assess whether LAE2 is spatially resolved in the MUSE data, we modelled the Lyα surface-brightness distribution of the system. The Lyα map was constructed by integrating the flux spaxel-by-spaxel over the velocity range $[-250, +750]$ km s^{-1} with respect to the systemic velocity of LAE2 (Fig. 5). This velocity interval encompasses the full Lyα emission of LAE2 (and LAE1) while minimising contamination from noise in the wings of the line. We note however that this range does not contain the blueshifted Lyα emission associated with GS10578 (see Fig. 9 in Perna et al. 2025).

We first modelled the Lyα flux distribution with three two-dimensional Gaussian components corresponding to the three sources in the field (LAE2, LAE1, and GS10578). The best-fit solution yields Gaussian profiles with FWHM$_x \simeq$ FWHM$_y \simeq 1''$ for all three sources, consistent with the angular resolution of the MUSE observations (FWHM$_{\rm PSF} \approx 0.7''$ at ~ 7000 Å observer-frame, and decreasing at lower wavelengths). No significant ($> 2\sigma$) residuals are found in the immediate vicinity of LAE2, indicating that its Lyα emission is consistent with an unresolved source at the resolution of MUSE. In contrast, significant residual emission is detected around LAE1 and GS10578, tracing an extended Lyα nebula associated with the system and elongated roughly along the north–south direction over a projected scale of ~ 50 kpc (see also Fig. 1).

As an alternative parameterisation, we also fitted the Lyα map using Sérsic profiles for the three components. This model provides a satisfactory description of the data, with no residuals exceeding $\pm 2\sigma$ in the vicinity of all the sources. The best-fit Sérsic indices are $n \simeq 0.5$ for LAE2 and $n \simeq 1$ for LAE1 and GS10578. The ellipticity and position angle of all three sources are consistent with circular profiles. The effective radius of LAE2 is $r_{\rm eff} \simeq 0.4''$, which is smaller than the MUSE PSF and therefore consistent with an unresolved source. In contrast, LAE1 and GS10578 have larger effective radii of $r_{\rm eff} \simeq 1.6''$, reflecting the contribution of the surrounding nebula to their surface-brightness distribution. Figure A.1 shows the Lyα flux distribution, the best-fit models, and the corresponding residual maps, for both 2-dimentional Gaussians (top panels) and Sérsic profiles (bottom panels).

Taken together, the Gaussian and Sérsic modelling results indicate that the Lyα emission associated with LAE2 is unresolved at the spatial resolution of the MUSE data. This interpretation is further supported by the fact that both NIRCam F200W imaging and NIRSpec-IFS observations show that the [O III] emission in LAE2 is approximately a factor of two less extended than the Lyα emission seen in the MUSE data. High ionisation lines as He II and C IV are detected at lower S/N in the MUSE cube, preventing any additional morphological analysis. We therefore treat LAE2 as spatially unresolved in the MUSE observations throughout this work.

Appendix B: Spectral energy distribution of LAE2 and LAE1

To characterise the stellar populations of LAE2 and explore potential constraints on LAE1, we attempted SED fitting using the available broadband photometry from archival HST and JWST imaging. We used the available archival HST (ACS/WFC F435W, F606W, F775W, F814W) and JWST/NIRCam imaging (F090W, F115W, F150W, F182M, F200W, F277W, F335M, F356W, F410M, F444W) from the JADES survey (Eisenstein et al. 2026; Rieke et al. 2023; Eisenstein et al. 2025). We PSF-matched all maps to the reddest filter (NIRCam's F444W band, with a measured PSF FWHM of $0.16''$) to enable consistent aperture photometry across wavelengths. We masked a nearby star located $\sim 2''$ from the system prior to photometric extraction to reduce contamination.We did not include JWST/MIRI data in the SED analysis, as both LAE2 and LAE1 remain undetected in these bands, and the relatively shallow MIRI exposures (Alberts et al. 2024) do not provide meaningful additional constraints on the fits.

For LAE2, we extracted aperture photometry using an elliptical aperture optimized to capture the source's morphology while maximizing S/N. LAE2 is detected in 13 filters (average S/N ~ 7.5), including 7 strong detections (S/N ~ 11) and 6 tentative detections (S/N ~ 3). For LAE1, located $0.9''$ ($\sim$7 kpc) east from LAE2, we applied a similar elliptical aperture centred on the position of the Lyα emission identified in MUSE for LAE1. Despite the depth of the JWST imaging, LAE1 shows no continuum detections in any filter, yielding only upper limits across all bands.

We fitted the observed photometry using the Code Investigating GALaxy Emission (`CIGALE`; Boquien et al. 2019), a Bayesian SED fitting code that models panchromatic galaxy emission. We first fitted LAE2, given its multiple continuum detections, and then attempted to constrain LAE1 despite the lack of detections.

We adopted model components and priors tailored to the AGN-hosting nature of LAE2. For the star formation history (SFH), we used delayed exponentially declining models with SFR$(t) \propto t \exp(-t/\tau)$, with e-folding times τ kept as free parameter. Stellar populations were modelled using Bruzual & Charlot (2003) templates with Chabrier (2003) IMF and sub-solar metallicities. Nebular emission was computed using Cloudy models with ionisation parameter log$U$ ranging from -3 to -1 (spanning star-forming to AGN-dominated ionisation regimes). We fixed the nebular line widths to 112 km s^{-1} based on our spectroscopic measurements (Table 1). The Lyman continuum escape fraction was allowed to vary from 0 to 0.3, consistent with the constraints derived from the Lyα/Hα ratio (4).

Dust attenuation was modelled using a modified Calzetti et al. (2000) law with colour excess E(B-V) ranging from 0 to 0.03 mag, appropriate for low-attenuation systems like LAE2. We allowed the slope of the attenuation curve to vary between -2 and 2. Given the confirmed AGN nature of LAE2 (Sect. 4), we included Fritz et al. (2006) clumpy torus models in our SED fitting analysis. We sampled optical depths at 9.7 microns ranging from 0.3 to 10, torus opening angles between 60 and 140 degrees, and three viewing angles corresponding to face-on, intermediate, and edge-on configurations (Type 1, intermediate, and Type 2 AGNs). We adopted the Schartmann et al. (2005) disk spectrum, and dust temperatures between 100 and 300 K.

For LAE1, given the absence of continuum detections, we adopted a different strategy to enable SED fitting. We treated the reddest band (F444W, S/N ~ 2) as a detection to provide a minimal anchor point for `CIGALE`, while all other filters were kept as upper limits. We applied the same model components and priors as for LAE2, but excluded the AGN scenario since with only upper limits, we cannot constrain complex models. Although attempting to forge an SED for LAE1 is speculative, it allows us to derive upper limits on the assumed stellar mass and SFR. Given the lack of detections, the resulting SED fit represents stringent constraints rather than physical measurements.

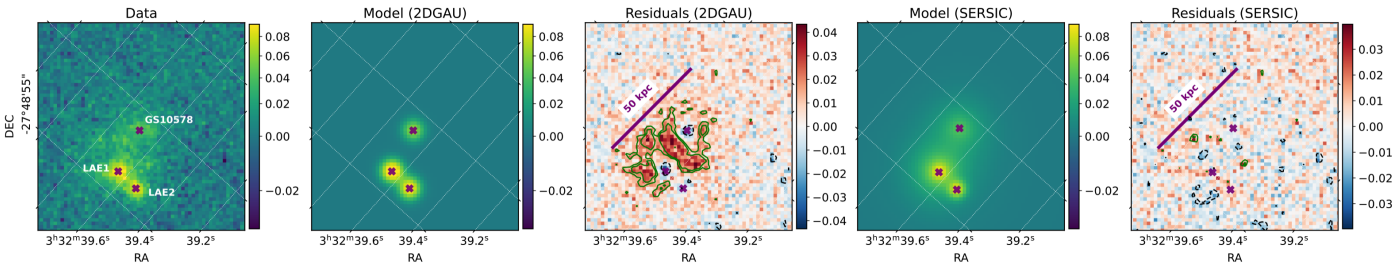

Fig. A.1. Modelling of the Lyα flux distribution in the MUSE data. From left to right: Lyα flux map; best-fit model using three 2D Gaussian components representing LAE2, LAE1, and GS10578; residual map after subtraction of the Gaussian model; best-fit model using three Sérsic profiles; residual map after subtraction of the Sérsic model. Flux units in 10^{-17} erg s^{-1} cm^{-2}; in the residual maps, contours indicate levels of -2σ (dashed black) and $+3\sigma$ and $+4\sigma$ (solid green). The Gaussian model yields FWHM values consistent with the MUSE angular resolution, indicating that LAE2 is spatially unresolved, while significant residuals around LAE1 and GS10578 in the central panel traces the extended Lyα nebula associated with the system. The Sérsic model provides a satisfactory description of the data, with no residuals.

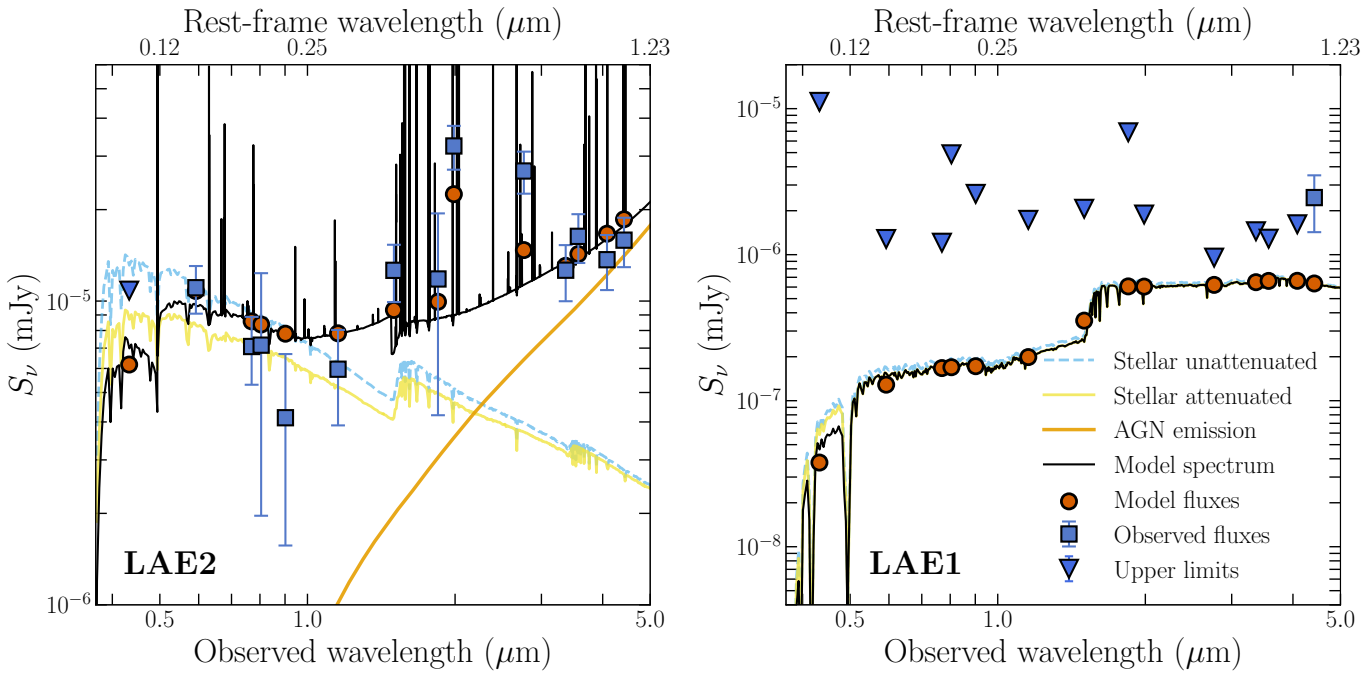

Fig. B.1. Best-fit spectral energy distributions for LAE2 (left) and LAE1 (right), computed using the configuration described in B. The observed photometry (blue squares for detections, blue triangles for 3σ upper limits) spans HST/ACS through JWST/NIRCam. For LAE1, the reddest point is marked with a square, because used as an anchor point for the SED fit, but represents an upper limit. Model fluxes are shown as red circles. The solid black line shows the total model spectrum, while coloured lines indicate individual components. The top axis shows rest-frame wavelength at $z = 3.07$.

Table B.1. Physical properties from SED fitting for LAE2 and LAE1.

Property	LAE2	LAE1 (upper limits)
$\log(M_\star/M_\odot)$	$7.78^{+0.18}_{-0.32}$	$6.19^{+0.18}_{-0.32}$
SFR [$M_\odot$ yr^{-1}]	0.13 ± 0.07	0.02 ± 0.03
$f_{\rm AGN}$	0.40 ± 0.17	—
Age [Myr]	416 ± 162	158 ± 55
A_V [mag]	0.07 ± 0.05	0.02 ± 0.01
Z [$Z_\odot$]	0.16 ± 0.13	0.14 ± 0.09
$\log U$	-1.39 ± 0.49	-2.50 ± 0.41

Notes. Errors represent 68% confidence intervals (16th-84th percentiles). LAE2 was fitted with stellar+AGN model; LAE1 with stellar-only model. LAE1 results represent upper limits given the lack of continuum detections.

The computed SED for LAE2 and LAE1 are shown in Fig. B.1, and the resulting physical properties corresponding to these best fit solutions are shown in Table B.1. The SED fitting results confirm that LAE2 is a low-mass galaxy ($\log(M_\star/M_\odot) = 7.78^{+0.18}_{-0.32}$, with a young stellar population (age $\approx$ 415 Myr, corresponding to formation at $z \sim 3.5$–4) and modest ongoing star formation (SFR ≈ 0.13 M$_\odot$ yr^{-1}, consistent with estimates based on Balmer lines in Sect. 5.3). The derived AGN fraction of $f_{AGN} = 0.4 \pm 0.2$ confirms that AGN emission contributes significantly to the total infrared luminosity. For LAE1, the SED fit yields only weak constraints given the absence of continuum detections. The inferred stellar mass upper limit ($\log(M_\star/M_\odot) \lesssim 6.5$) and very low SFR ($\lesssim 0.02$ M$_\odot$ yr^{-1}) are consistent with LAE1 being either an extremely low-mass, metal-poor dwarf galaxy or dominated by scattered Lyα emission with no stellar contribution, as suggested by the spectroscopic analysis.